This is a preprint, the final version is subject to change, of the American Mineralogist (MSA)
Cite as Authors (Year) Title. American Mineralogist, in press.
DOI: http://dx.doi.org/10.2138/am-2018-6087

Revision 3: Crystal Structure of $CaSiO_3$ Perovskite at 28–62 GPa and 300 K under Quasi-hydrostatic Stress Conditions

Huawei Chen[1,*], Sang-Heon Shim[1], Kurt Leinenweber[2], Vitali Prakapenka[3], Yue Meng[4], and Clemens Prescher[3,5]

[1]School of Earth and Space Exploration, Arizona State University, Tempe, Arizona 85287-1404, U.S.A.

[2]School of Molecular Sciences, Arizona State University, Tempe, Arizona 85287-1604, U.S.A.

[3]GeoSoilEnviroCars, University of Chicago, Chicago, Illinois 60439, U.S.A.

[4]HPCAT, Carnegie Institution of Washington, Argonne, Illinois 60439, U.S.A.

[5]Institut für Geologie und Mineralogie, Universität zu Köln, Köln 50674, Germany.

Abstract

In order to find the thermodynamically stable crystal structure of $CaSiO_3$ perovskite (CaPv) at high pressure and 300 K, we have conducted synchrotron X-ray diffraction (XRD) on thermally stress-annealed samples in a Ne pressure medium in the diamond-anvil cell at 28-62 GPa. Rietveld refinements of the diffraction patterns are significantly improved in fitting the positions and intensities of the split lines of CaPv if the starting model is a tetragonal perovskite-type structure with the SiO_6 octahedral rotation around the tetragonal *c*-axis. The result is in contrast with other previous

*Corresponding author: Huawei Chen, hchen156@asu.edu

experiments, but is consistent with first-principles calculations, reconciling the discrepancy between computations and experiments on the crystal structure of CaPv. We attribute the observed difference to the formation of the thermodynamically more stable phase under improved stress conditions in our experiments. Our fitting shows that the bulk modulus of Ca-Pv is 223±6 GPa when its pressure derivative fixed to 4, which is also consistent with first-principles calculations. The previous observations of the diffraction patterns of CaPv inconsistent with the first-principles studies could be due to the formation of a metastable crystal structure of CaPv under elevated deviatoric stresses.

Keywords: $CaSiO_3$ perovskite; crystal structure; hydrostatic stress; X-ray diffraction; equation of state.

Introduction

Perovskite-structured $CaSiO_3$ (hereafter CaPv) is the third most abundant mineral (5–7 wt%) in the pyrolitic model composition of the Earth's mantle (Kesson et al. 1998; Murakami et al. 2005; Ricolleau et al. 2009). CaPv is stable over a wide depth range from the transition zone to the lowermost mantle (Shim et al. 2000; Ohta et al. 2008). In mid-oceanic ridge basalt (MORB) in subducting slabs at lower-mantle pressures, CaPv represents 23 wt% of the mineralogy, comparable to the amount of bridgmanite, that is 35 wt% (Hirose et al. 2005; Ricolleau et al. 2010, Grocholski et al. 2012).

Existing studies are in agreement in that CaPv has a phase transition from a non-cubic to a cubic perovskite-type structure with heating (T >500 K) (Komabayashi et al. 2007; Noguchi et al. 2013; Sun et al. 2016) at pressures (P) expected for the lower

mantle. However, there remain significant discrepancies between computations and experiments on the crystal structure of the lower-temperature form of CaPv and its compressibility. In the 1980s, it was believed that CaPv adopts the cubic perovskite structure ($Pm\bar{3}m$) at 300 K and lower mantle pressures from energy-dispersive X-ray diffraction (Liu and Ringwood 1975; Mao et al. 1989; Tamai and Yagi 1989; Wang et al. 1996). *Ab initio* calculations first predicted a lower symmetry structure for CaPv. Stixrude et al. (1996) found the instability of the cubic structure with a SiO_6 octahedral rotation of 7 degrees towards the tetragonal *I*4/*mcm* subgroup. Caracas et al. (2005) performed a more exhaustive search for the ground state of CaPv and tetragonal *I*4/*mcm* was regarded as one of the most energetically competitive structures at low temperature and high pressure.

Using high-resolution angle-dispersive diffraction technique, Shim et al. (2002) found a non-cubic unit cell for CaPv at 20-46 GPa and 300 K. However, they found that the positions and intensities of the split peaks (in particular the 200_{pc} peak, where the subscript "*pc*" represents the Miller indices referred to the cubic aristotype unit cell of perovskite) are more consistent with a longer *a*-axis than *c*-axis ($c_{pc}/a_{pc} < 1$). The ratio is opposite to what is expected for the crystal structures predicted by computations, which predicted the octahedral rotation ($c_{pc}/a_{pc} > 1$) as an origin of the non-cubic structure. Instead, the experimental observation is more straightforward to understand if one of the three axes of the SiO_6 octahedra is shorter than the other two (therefore, direct distortion of the octahedra). Later XRD studies have shown a similar pattern of the 200_{pc} peak splitting as Shim et al. (2002) in $CaSiO_3$ (Komabayashi et al. 2007; Sun et al. 2016), peridotite (Ono et al. 2004) and MORB (Hirose et al. 2005) compositions at room

(ambient) *T* and high *P*. A multi-anvil press experiment identified an orthorhombic CaPv at *P*-*T* up to 20 GPa and 1600 K (Uchida et al. 2009). However, such a low symmetry phase in CaPv has not been identified at higher pressures. Therefore, the discrepancy between theory and experiments remain unresolved for the stable crystal structure of CaPv at 300 K and high pressure.

The rotations of the rigid octahedra are responsible for the low-symmetry crystal structures of a wide range of perovskite-structured materials (Glazer 1975; Woodward 1997). For example, the rotation of the framework octahedra in a cubic perovskite structure can result in a number of lower symmetry structures, including three tetragonal subgroups, *I*4/*mcm*, *P*4/*mbm,* and *I*4/*mmm*. Rotation along the *c*-axis can lead to the *I*4/*mcm* and *P*4/*mbm* structures with $c_{pc}/a_{pc} > 1$, as the rotation reduces the dimension in the (110) plane. In the case of the *I*4/*mmm* structure, rotation around the *a* axis can result in $c_{pc}/a_{pc} < 1$. This symmetry also allows for octahedral distortion during the rotation. Because of this relationship between the axial ratio and the crystal structure, Shim et al. (2002) found that the observed $c_{pc}/a_{pc} < 1$ is difficult to explain with the octahedral rotation alone and some degree of the octahedral distortion should be invoked. Therefore, they use *P*4/*mmm,* which is purely based on the octahedral distortion along the *c*-axis, as a proxy to explore the possibility for the distorted octahedra case. In *P*4/*mmm*, the Si-O bonds along the *c*-axis are shorter than the bond along the *a*-axes in a tetragonal unit cell. From the strong Si-O bonding, it is surprising that CaPv has a lower symmetry structure through the direct distortion of the octahedra, which would require more energy than the rigid octahedral rotation. Also, *P*4/*mmm* structured perovskites are much less common than many other subgroups (Comyn et al. 2004).

It is possible that the measured crystal structure of CaPv is sensitive to the deviatoric stresses in diamond-anvil cell (DAC). Most experimental studies on CaPv have been conducted in DACs where pressure medium play an important role for the stress conditions of the sample. Earlier studies used Ar (Shim et al. 2002) or MgO (Kurashina et al. 2004; Komabayashi et al. 2007) as pressure media, but some were conducted even without a pressure medium (Ono et al. 2004, 2005). All these studies have observed non-cubic CaPv (*P*4/*mmm*) upon temperature quench. Although laser annealing reduces the deviatoric stress in a DAC, 40–80% of stress can be reintroduced upon temperature quench in a MgO pressure medium (Kavner and Duffy 2001). Because computational studies have shown that differences of free energy among competing crystal structures are very small (Caracas et al. 2005), it is important to reduce the effects from non-equlibrium conditions, such as deviatoric stresses, as much as possible. In this study, we use Ne as a pressure medium combined with laser annealing to 1,700-2,300 K in order to measure the stable crystal structure of CaPv under quasi-hydrostatic stress conditions at 300 K and high pressures.

Experimental procedures

We synthesized a $CaSiO_3$ glass using the laser levitation method (Tangeman et al. 2001) for a starting material. We measured the composition of the glass using wavelength dispersive X-ray spectrometry (WDS) in an electron probe microanalyzer (EPMA; JXA-8530F) at Arizona State University. The glass starting material has a Ca/Si molar ratio of 0.993±0.009 and is compositionally homogeneous.

The glass starting material was mixed with 10 wt% platinum (99.98% purity with a grain size less than 3 μm; Alfa Aesar). We used platinum as an internal pressure standard (Ye et al. 2017) and a laser absorber. The sample+Pt powder mixture was pressed into a foil and loaded into a chamber drilled in a Re gasket with the diamond anvils mounted on symmetric-type DAC. We used 400 μm culet diamond anvils for a peak pressure less than 35 GPa, and 200 μm culet diamond anvils for experiments above this pressure. We loaded Ne using the gas-loading system at the GSECARS sector as a pressure transmitting medium and thermal insulator (Rivers et al. 2008). Small $CaSiO_3$ glass grains (diameter < 10 μm and thickness < 2 μm) were placed below and above the sample foil, in order to allow Ne to flow above and below the sample foil in the sample chamber during the gas loading. This setup ensures that Ne forms layers between the sample and the diamond anvils for thermal insulation. In one experiment, we loaded the starting material without any medium, in order to examine the effects of deviatoric stress and thermal gradients.

We measured XRD patterns at in-situ high *P-T* in the laser heated DAC at beamlines 13ID-D in the GSECARS sector (Prakapenka et al. 2008) and 16ID-B in the HPCAT sector (Meng et al. 2006) at the Advanced Photon Source. Monochromatic X-ray beams with beam sizes of 3×4 and 5×6 μm^2 at GSECARS and HPCAT, respectively, were focused on the sample and the diffraction patterns were collected using a Mar-CCD detector. We focused near-infrared laser beams (1-μm wavelength) on the sample with a hot spot size of 20-25 μm in diameter and aligned them coaxially with the X-ray beam (Meng et al. 2006; Prakapenka et al. 2008). We measured the temperature of the heated

spots by fitting Planck equation to the thermal radiation spectra from both sides of the sample after subtracting the effects of the optical systems.

Before laser heating, we confirmed the amorphous state of $CaSiO_3$ glass through XRD. In a typical experiment, we compressed the sample to target pressures at 300 K, and then heated a spot on the sample foil for approximately 5 minutes. We increased the laser power to the target temperature (1,700-2,300 K) within 1 minute to avoid the possible synthesis of metastable phases at low temperatures. We measured several XRD patterns during and after heating. CaPv forms within 1 minute upon heating above 1,700 K. The diffraction pattern of CaPv remains essentially the same during heating after the formation. After temperature quench, we acquired diffraction patterns on the stress annealed spot at high pressure.

It is challenging to detect the subtle peak splitting in a quasi-hydrostatic pressure medium. Therefore, we have optimized X-ray energy and detector-sample distance to achieve the maximum resolution of the systems we used. Our maximum resolution was achieved at a detector distance of 249.92 mm for an X-ray energy of 25 keV. The use of a low-energy X-ray beam limited the measurable *d*-spacing to >1.557 Å, but enabled us to detect the peak splitting of the 200*pc* line from CaPv.

We used the software package Dioptas (Prescher and Prakapenka 2015) to integrate the 2D diffraction images to 1D diffraction patterns. We identified phases and measured full width at half maximum (FWHM) of XRD peaks by the software PeakPo (Shim 2017). The data obtained from the GSECARS and HPCAT beamlines agreed well with each other for the peak positions and intensities of CaPv. We performed Rietveld refinements of the XRD patterns using the general structure analysis system (GSAS)

159 software combined with EXPGUI (Toby 2001). We refined the phase fractions first, then
160 the atomic positions, the lattice parameters and the spherical harmonic terms for the
161 preferred orientation. After reaching a good visual fit, we refined all the parameters
162 together to minimize the fit residuals.

163 A few different possible crystal structures have been proposed for CaPv at low
164 temperature and high pressures (Stixrude et al. 1996, 2007; Akber-Knutson et al. 2002;
165 Shim et al. 2002; Caracas et al. 2005; Jung and Oganov 2005; Adams and Oganov 2006;
166 Caracas and Wentzcovitch 2006; Li et al. 2006; Uchida et al. 2009). The focus of our
167 experiments presented here is: should the direct distortion of the SiO_6 octahedra (for
168 example, *P*4/*mmm* in Shim et al. 2002) be invoked in order to explain the diffraction
169 patterns from the CaPv phase stable at high pressure and 300 K? Or is the octahedral
170 rotation (for example, *I*4/*mcm* in Stixrude et al. 2007) sufficient as has been shown in the
171 computation and seen from a wide range of perovskite-structured materials?

172 In order to demonstrate the differences in powder diffraction patterns, we
173 conducted calculations using the crystal structures proposed for CaPv (Figure 1) (Shim et
174 al. 2002; Caracas and Wentzcovitch 2006). The cubic 200 diffraction line of CaPv splits
175 the most in both tetragonal diffraction patterns (*P*4/*mmm* and *I*4/*mcm*). However, the
176 relative intensities of the two split lines from the 200_{pc} peaks differ depending on the
177 space groups. For example, the lower-angle diffraction line (004 in Figure 1) has a lower
178 intensity in *I*4/*mcm*, while it has a higher intensity in the *P*4/*mmm* structure (200 in
179 Figure 1). More importantly, the higher 2θ-angle split line of 200_{pc} existed at a similar
180 angle as the original cubic 200 line for the octahedral rotation cases. However, for the
181 octahedral distortion case, it is the lower angle split line that exists at a similar 2θ angle

as the cubic 200 line (*P*4/*mmm*). These peak position differences are related to the fact that through the rotations of the SiO_6 octahedra in the (001) plane, the c_{pc} axis becomes longer than the a_{pc} axis in the *I*4/*mcm* structure, resulting in $c_{pc}/a_{pc} > 1$. Although the *I*4/*mcm* structure does not result in $c_{pc}/a_{pc} < 1$, shorter Si-O bonding distances in the octahedra can make the c_{pc}/a_{pc} ratio is smaller than 1 in the *P*4/*mmm* space (Shim et al. 2002). Therefore, for $c_{pc}/a_{pc} < 1$, as observed by Shim et al. (2002), it is difficult to explain the crystal structure of CaPv with the octahedral rotation alone and some degree of octahedral distortion (shorter Si-O bonding along the *c* axis) needs to be invoked. According to our calculation, the cubic 110, 211, and 220 diffraction peaks also show splitting but with smaller degrees in both *I*4/*mcm* and *P*4/*mmm* structures. Therefore, the splitting of these latter lines is more difficult to resolve.

While the peak splitting of the relatively intense lines are helpful to distinguish the octahedral distortion (*P*4/*mmm*) versus octahedral rotation (*I*4/*mcm* and *P*4/*mbm*), the presence and absence of some lines could further help to distinguish these two possibilities. Also, those weak diffraction features would help to further distinguish a range of different symmetries possible for the octahedral rotation case, such as *I*4/*mcm*, *P*4/*mbm*, and *I*4/*mmm*. However, the weak diffraction lines are difficult to detect convincingly through powder diffraction in DAC. Although our 2D diffraction images show some weak spots in those angular ranges, it is difficult to unambiguously assign them to the diffraction peaks of CaPv because they could result also from other materials along the beam path, such as beam stoppers, X-ray optics, and X-ray guides. Such task can be better addressed through multi-grain diffraction (Margulies et al. 2001; Nisr et al. 2012) or single crystal diffraction techniques. Therefore, for our powder diffraction study

205 presented here, we focus on peak splitting and their implications for the octahedral
206 rotation versus octahedral distortion.
207
208 **Results and Discussion**
209 During laser heating, we did not observe any splitting of the CaPv diffraction lines
210 at temperatures between 1,700 K and 2,300 K up to our highest resolution XRD setup (X-
211 ray wavelength = 0.4959 Å and sample-to-detector distance = 197.52 mm) (Figure 2).
212 The observations support the stability of the cubic structure at high temperatures as
213 proposed by previous studies (Ono et al. 2004; Stixrude et al. 2007; Kurashina et al.
214 2004).
215 After temperature quench, we observed the clear splitting of the CaPv 200_{pc} line
216 (Figure 2a) at pressures between 28 and 62 GPa. In the 2D diffraction images (Figure 2c),
217 we also observed diffraction spots split into two. This shows that the symmetry change
218 occurs during temperature quench.
219 Unlike previous experiments (Shim et al. 2002; Kurashina et al. 2004; Komabayashi
220 et al. 2007), we found that the higher-angle diffraction line of the split 200_{pc} line has a
221 greater intensity throughout our studied pressure range at 300 K in both 2D and 1D
222 diffraction data (Figures 2a and c). As shown in Figures 1b and 2a, our new results is
223 more consistent with the XRD patterns expected for the tetragonal structures induced by
224 octahedral rotation (such as, *I*4/*mcm*), which has been proposed by first-principles
225 calculations (e.g., Stixrude et al. 1996, 2007; Caracas et al. 2005), than octahedral
226 deformation (*P*4/*mmm*), which has been indicated by previous XRD experiments (e.g.,
227 Shim et al. 2002; Kurashina et al. 2004; Komabayashi et al. 2007).

Diffraction intensities can be strongly affected by preferred orientation in powder samples in the DAC. Preferred orientation can be caused by such effects as plastic flow and preferential twinning, in response to the stress field. These effects can be reduced when deviatoric stress is minimized. We performed Rietveld refinements with fitting for the preferred orientation. We refined the diffraction patterns measured under our best resolution setup (Figure 3). These refinements were performed with two different crystal structures for CaPv: *I*4/*mcm* (the octahedral rotation, Stixrude et al. 1996) and *P*4/*mmm* (the octahedral deformation, Shim et al. 2002) (Table 1). In order to facilitate the comparison, we used the same parameters for the background in the fitting with the *I*4/*mcm* and *P*4/*mmm* starting structural models of CaPv.

Even when we fitted up to 14 parameters in a spherical harmonic function, we found significant mismatch between measured and calculated intensities of 200_{pc} and 211_{pc} for the octahedral distortion case (Figure 3b). We found significantly better fits for the octahedral rotation case. The improvement is mainly because the octahedral rotation requires the higher-2θ split line to be closer in peak position to that of the cubic 200_{pc} line. In contrast, the octahedral distortion requires the lower-2θ split line to be closer in peak position to that of the cubic 200_{pc} line. Therefore, if the observed diffraction is more consistent with the octahedral rotation, the fit with the octahedral distortion would result in large positive residue at the lower-angle side of the 200_{pc} split lines. The expected positive residue can be indeed found in Figure 3b. In other words, the intensity residual for the 200_{pc} line is significantly impacted by the relative position of the split lines (and therefore the *c*/*a* ratio), which is not sensitive to the preferred orientation, as well as the intensities of the split lines, which is sensitive to the preferred orientation.

From our Rietveld refinements, we obtained the c_{pc}/a_{pc} of CaPv (Figure 4). The c_{pc}/a_{pc} remains constant within the pressure range we studied. Therefore, we averaged c_{pc}/a_{pc} over our pressure range and the value is 1.0054±0.0005. Shim et al. (2002) showed that the octahedral rotation will lead to a c_{pc}/a_{pc} higher than 1, while the ratio can be either greater or smaller than 1 for the octahedral distortion depending on the shape of the SiO_6 octahedra. Shim et al. (2002) reported 0.995, which cannot be explained by the octahedral rotation alone but requires octahedral distortion. However, in our study, we found that the c_{pc}/a_{pc} value is higher than 1, suggesting octahedral rotation as the main source of symmetry lowering in CaPv. In other words, it is not necessary to invoke direct deformation of the octahedra, which is less common among perovskite-structured materials (Woodward et al. 1997).

Based on *ab initio* calculation, Stixrude et al. (2007) suggested an increase in c_{pc}/a_{pc} from 1.013 to 1.020 with an increase in pressure from 1 bar to 140 GPa at 0 K from the octahedral rotation. Because our pressure range is smaller, such a small increase per unit of pressure would be difficult to resolve from our data. On the other hand, because the value from the *ab initio* calculation is performed for 0 K, thermal effects could further decrease c_{pc}/a_{pc}. Stixrude et al. (2007) estimated that the value would decrease to 1.0094 at 25.2 GPa and 300 K, which is more similar to our new results.

As indicated by Caracas et al. (2006), several competing structures can explain c_{pc}/a_{pc} greater than 1 based on octahedral rotation, such as *I*4/*mcm*, *P*4/*mbm* or *I*4/*mmm*, all of which cause the elongation of the *a*-axes. Because of the subtle differences in their expected diffraction patterns as discussed earlier and the limitation of power XRD, the space group of the CaPv at 300 K and high pressure remains uncertain. The space group

*I*4/*mcm* is a reasonable option because it is known to occur as an intermediate distortion between the aristotype $Pm\bar{3}m$ and the common *Pbnm* orthorhombic distortion, including for example in the prototype compound $CaTiO_3$ (Yashima and Ali, 2009).

Using our Rietveld results with the *I*4/*mcm* structure, we fit the pressure–volume data at 300 K to the Vinet equation (Vinet et al. 1989). Using the Pt scale of Ye et al. (2017), we obtained an isothermal bulk modulus of 223(6) GPa (Table 2). In the fitting, we fixed the pressure derivative of the isothermal bulk modulus (B_0') to 4.0, while we also fit the volume at 1 bar and 300 K (V_0), because CaPv is unstable at these conditions and therefore V_0 is unknown. From the fitting we obtained V_0 = 46.3(1) Å^3.

Former studies have used the V_0 value projected through the extrapolation of CaPv equation of state (EOS) measured between 0.59 and 10.07 GPa by Wang et al. (1996). We also conducted fitting for the bulk modulus with V_0 fixed to the value by Wang et al. (1996). As shown in (Figure 5c), we found severe misfit for our data points below 35 GPa as well as the data points from Shim et al. (2002) at the similar pressure range. We also attempted fitting B_0 and B_0' by fixing V_0 to the value by Wang et al. (1996). However, we found unusually low B_0' (2.3) for B_0 = 290 GPa with much larger fit residual.

Although Wang et al. (1996) measured most of the data points of CaPv outside of the stable pressures, all of our data points are measured within the stability field of CaPv. For the case of bridgmanite, Wang et al. (1994) discussed that the phase may show abnormal volume behavior and such effects appear to be particularly severe near the conditions where the phase is amorphized. We note that CaPv amorphizes as pressure approaches 1 bar. It cannot be ruled out that CaPv may have different crystal structure

297 outside of its stability field because of the subtle free energy differences among candidate
298 structures and subtle differences in their expected XRD patterns. We note that Wang et
299 al. (1996) used a cubic perovskite structure to fit their data.

300 Our bulk modulus value is consistent with the computational studies (Table 2)
301 (Chizmeshya et al. 1996; Akber-Knutson et al. 2002; Magyari-Köpe et al. 2002; Jung and
302 Oganov 2005). If the thermal effect is taken into consideration, the bulk modulus of CaPv
303 at 300 K based on the 0 K value from some theoretical studies (such as, Caracas et al.
304 2005; Stixrude et al. 2007; Kawai and Tsuchiya 2014) would become more similar to our
305 value and therefore are also consistent with our results.

306 We compare our data points with those from Shim et al. (2002) in Figure 5. In this
307 comparison, we use the Pt and Au pressure scales by Ye et al. (2017), which are inter-
308 calibrated and consistent with each other within ±1 GPa. Our new EOS agrees well the
309 data from Shim et al. (2002) at 20-60 GPa. Two experimental studies have reported the
310 zero-pressure bulk modulus of CaPv projected from its cubic stability field (>700 K): 249
311 GPa from Sun et al. (2016) and 225 GPa from Noguchi et al. (2013). The latter is more
312 consistent with our value based on measurements performed directly at 300 K. The
313 discrepancy between two high temperature studies may be because they need
314 extrapolation and the bulk modulus can be also changed by the crystal structure. In
315 addition, in EOS fitting, strong correlation among fit parameters can result in differences,
316 and thermal gradients can contribute to the uncertainties.

317 In this study, we improve the stress conditions of experiments for CaPv by
318 combining a soft pressure medium (Ne) and laser annealing. The improved stress
319 conditions in our new experiments may be important for explaining the different results

we obtained in this study. In order to test this hypothesis, we conducted a laser-heated DAC experiment for the same starting material but without a pressure medium. In this "no medium" experiment, we found that the CaPv 200_{pc} diffraction peak is much broader and much more asymmetric than runs with Ne both during and after laser heating (Figure 6). We note that even at 1550 K 200_{pc} shows splitting at 31 GPa. The peak width of CaPv 200_{pc} without a medium is a factor of 2.3 greater than that in a Ne pressure medium at similar *P-T* conditions (Figure 6). We also find that other lines have asymmetric peak shapes, which were not observed in our experiments with a Ne medium. Because thermal annealing does not relieve the deviatoric stress completely (Kavner and Duffy 2001), some degree of deviatoric stresses still remain in our "no-medium" experiments likely to much higher degree than our Ne medium experiments. Therefore, we interpret that the non-hydrostatic stresses cause the broadening and splitting of the 200_{pc} peak in the "no medium" experiments.

We estimate pressures from individual diffraction lines of Pt. For the experiments with a Ne medium and laser annealing, we obtain -0.5~2.5 GPa differences in pressure between the 111 and 200 lines of Pt. The value is comparable to that reported for laser-annealed Pt in a Ne medium by Ye et al. (2017) where they estimated unit-axial stress component (*t*) of -0.5~1.0 GPa. Instead, for the no medium data point, we found much a higher value for the pressure difference, 7.5 GPa. The elevated deviatoric stresses can affect the crystal structure of CaPv. They may enhance the existing distortions, or even induce different distortions and consequently stabilize a metastable structure.

It is also possible that the thermal gradients during the heating without an insulation medium and the pressure gradients remaining after heating would produce a range of

CaPv crystals with different degree of distortions or even with different crystal structures along the X-ray path. Indeed, the diffraction patterns are difficult to fit with the candidate structures we tried for the data measured in a Ne medium.

High shear strength pressure-transmitting media can support larger amounts of deviatoric stress in the DAC. Magnesium oxide (MgO), which is used for CaPv (Komabayashi et al. 2007), is a highly nonhydrostatic medium, with a 10 GPa shear strength at pressures between 60 and 100 GPa (Duffy et al. 1995). The shear strength of Ar, which was used in Shim et al. (2002), is about 0.8 GPa at 65 GPa when the stress is not thermally annealed, while thermal annealing at 700 K reduces the stress to 0.56 GPa at 65 GPa (Marquardt et al. 2013). The pressure gradient using a Ne medium is less than 0.5 GPa at a pressure of 50 GPa without annealing (Klotz et al. 2009).

In this study, we used cold compressed foils of the powdered starting material. Under a microscope, we found that the foil contains small pore spaces and cracks, which should allow significant amounts of Ne to penetrate the grain boundaries. We also found that the foils disintegrated during decompression to 1 bar. Therefore, we believe that the soft Ne medium should have controlled the stress field of individual CaPv grains in our experiment.

Although noble gas media in general support smaller deviatoric stresses, CaPv appears to be still sensitive to such smaller deviatoric stress in the media. The different crystal structures of CaPv, which are metastable in the stress-free state, can appear easily with small deviatoric stress, because of their similar free energies (Caracas et al. 2005).

366 **Implication**

367 Experimental and theoretical mineral physics studies on the properties of minerals
368 play an important role in understanding the structures and processes in the Earth's
369 interior. In theoretical studies, in order to compute the physical properties accurately, it
370 is important to know the stable crystal structures of the mantle phases. In this study, we
371 resolve long-standing discrepancy on the crystal structure of CaPv at 300 K and mantle-
372 related high pressure between theoretical and experimental studies. For experimentalists,
373 our finding of extreme sensitivity of CaPv on deviatoric stress highlights the importance
374 of conducting measurements on crystal structures and physical properties under better
375 controlled/characterized stress conditions relevant to those of the Earth's interior.
376

377 **Acknowledgments**

378 We thank two anonymous reviewers and Dr. Speziale for helping us to improve this
379 paper. The results reported herein benefitted from collaborations and/or information
380 exchange within NASA's Nexus for Exoplanet System Science (NExSS) research
381 coordination network sponsored by NASA's Science Mission Directorate. This work was
382 supported by NSF grants EAR1321976 and EAR1401270 to S.H.S. The synchrotron
383 experiments were conducted at GSECARS and HPCAT, Advanced Photon Source
384 (APS), and Argonne National Laboratory. GSECARS is supported by NSF-Earth Science
385 (EAR-1128799) and DOE-GeoScience (DE-FG02-94ER14466). HPCAT is supported by
386 DOE-NNSA (DE-NA0001974), DOE-BES (DE-FG02-99ER45775), and NSF. APS is
387 supported by DOE-BES, under contract DE-AC02-06CH11357. The experimental data

388 for EOS are available in Table 1. Other data for this paper are available by contacting

389 SHDShim@asu.edu.

390 Table 1: Structural parameters of CaPv determined by Rietveld refinements. The
391 numbers in the parentheses are 2σ uncertainties for the last digit. Pressure was
392 calculated from the Pt scale by (Ye et al. 2017).
393

Run#	*P* (GPa)	Structure	Tilting angle (°)	*a* (Å)	*c* (Å)
71013	28.824	*I*4/*mcm*	8.0(4)	4.8896(3)	6.9677(8)
		*P*4/*mmm*	0	3.4690(2)	3.4496(4)
81021	29.138	*I*4/*mcm*	8.6(7)	4.8941(1)	6.9546(4)
		*P*4/*mmm*	0	3.4685(3)	3.4582(5)
81030	32.307	*I*4/*mcm*	9.4(2)	4.8805(2)	6.9611(8)
		*P*4/*mmm*	0	3.4610(2)	3.4477(4)
71050	41.972	*I*4/*mcm*	10.2(1)	4.8351(1)	6.8683(3)
		*P*4/*mmm*	0	3.4297(1)	3.4134(2)
81066	47.878	*I*4/*mcm*	7.8(1)	4.8070(2)	6.8354(3)
		*P*4/*mmm*	0	3.4119(1)	3.3922(3)
81074	53.884	*I*4/*mcm*	9.2(3)	4.7870(2)	6.8065(4)
		*P*4/*mmm*	0	3.3978(2)	3.3784(4)
71088	62.477	*I*4/*mcm*	8(1)	4.7535(1)	6.7571(3)
		*P*4/*mmm*	0	3.3737(1)	3.3546(2)

394
395

Table 2: Compressibility of CaPv at high pressure and 300 K.

Refs	V_0 (Å^3)	B_0 (GPa)	B_0'	Symm.[a]	Notes[e]
		Experiments			
This work	46.3(1)	223(6)	4[d]	Tet.	300 K, V, Pt-Y, Ne
Wang et al. (1996)	45.58(4)	232(8)	4.8[d]	Cub.	300 K, BM, NaCl, NaCl
Shim et al. (2002)	45.58[d]	255(5)	4[d]	Tet.	300 K, BM, Pt-H, Ar
Shim et al. (2002)	45.58[d]	259(8)	4[d]	Tet.	300 K, V, Pt-Y, Ar
Ricolleau et al. (2009)[b]	45.60[d]	244(1)	4[d]	Tet.	300 K, BM, Au-F, Ne
Noguchi et al. (2013)[c]	45.80	225	4[d]	Cub.	300 K, BM, Pt-F, NaCl
Sun et al. (2016)[c]	45.4(1)	249(4)	4[d]	Cub.	300 K, BM, Pt-F, KCl/NaCl
		Computation			
Kawai and Tsuchiya (2014)	46.17	203.5	4.76	Cub.	1000 K, V, LDA
Magyari-Köpe et al. (2002)	45.69	216	4.82	Orth.	300 K, V, LDA
Chizmeshya et al. (1996)	45.62	227	4.29	Cub.	300 K, BM, LDA
Caracas et al. (2005)	44.537	249	4.09	Tet.	0 K, BM, LDA
Stixrude et al. (2007)	44.00	252	4.1	Tet.	0 K, BM, LDA
Jung and Oganov (2005)	46.89	219	4.08	Tet.	0 K, BM, GGA
Akber-Knutson et al. (2002)	45.90	228	4.3	Orth.	300 K, BM, VIB

Notes: The numbers in the parentheses are 2σ uncertainties for the last digit.
[a] Cub., Tet., and Orth. refer to cubic, tetragonal, and orthorhombic CaPv structures respectively.
[b] They used pyrolitic composition as a starting material.
[c] The values were projected from high temperature to 300 K and 1 bar.
[d] The values were fixed during EOS fitting.
[e] Temperature, EOS, Pressure scale or Computational methods, Pressure medium. V and BM refer to the Vinet and third order Birch-Murnaghan equations, respectively. Pt-H, Pt-Y refer to the Pt scales Holmes et al. (1989) and (Ye et al. 2017) respectively. Au-F and Pt-F refer to the Au and Pt scales by Fei et al. (2007). LDA (Local Density Approximation); GGA (Generalized Gradient Approximation); VIB (Variationally Induced Breathing.)

This is a preprint, the final version is subject to change, of the American Mineralogist (MSA)
Cite as Authors (Year) Title. American Mineralogist, in press.
DOI: http://dx.doi.org/10.2138/am-2018-6087

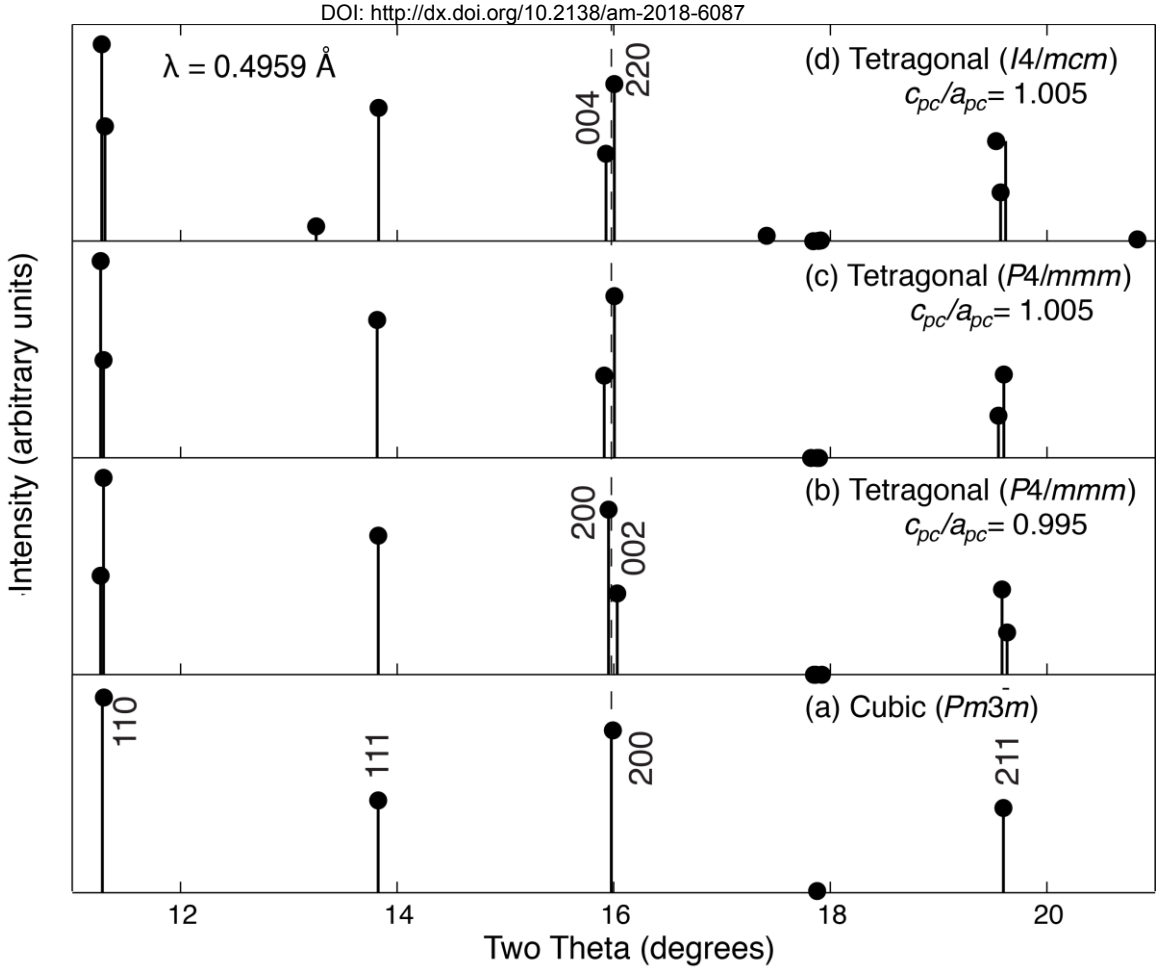

Figure 1: Calculated XRD patterns of CaPv in different crystal structures at 1 bar and 300 K (V_0 = 45.58 Å^3/Z, X-ray wavelength = 0.4959 Å): (a) cubic *Pm*$\bar{3}$*m* (Caracas and Wentzcovitch 2006) (b) tetragonal *P*4/*mmm* (*a* = 3.5781 Å and *c* = 3.5601 Å) (Shim et al. 2002) (c) tetragonal *P*4/*mmm* (*a* = 3.5662 Å and *c* = 3.5840 Å) and (d) tetragonal *I*4/*mcm* (*a* = 5.0426 Å and *c* = 7.1658 Å) (Caracas and Wentzcovitch 2006). In (a), the diffraction peaks are indexed with the cubic *Pm*$\bar{3}$*m* structure. For the tetragonal cases in (b-d), we assumed the same magnitude of deviation in the *c*/*a* ratio from 1: c_{pc}/a_{pc} = 0.995 for (b) and c_{pc}/a_{pc} = 1.005 for (c) and (d). The thin vertical dashed line extended from the 200_{pc} diffraction peak highlights the different angle shifts expected for the split lines in *I*4/*mcm* and *P*4/*mmm*.

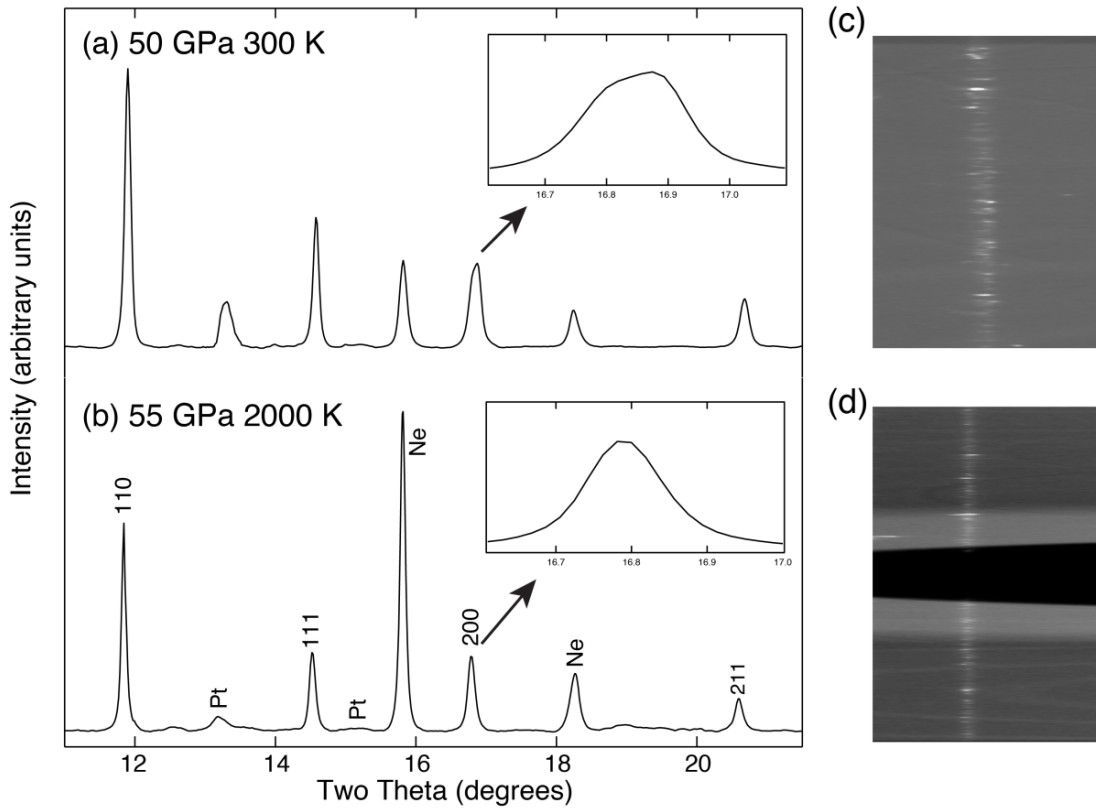

Figure 2: X-ray diffraction patterns of CaPv at 50-55 GPa and 300 K (a) and 2000 K (b). The samples include $CaSiO_3$ perovskite (CaPv), platinum (Pt, laser coupler) and neon (Ne, pressure medium). The peaks are indexed with the cubic $Pm\bar{3}m$ space group. The inset images show the (a) splitting and (b) no-splitting of the 200_{pc} diffraction peak at 300 K and 2000 K, respectively. The wavelength of the X-ray beam is 0.4959 Å. The unrolled projections of the 2D raw diffraction areas are shown for temperatures at (c) 300 K, and (d) 2000 K for the same 2θ range (1.2°). In (d), the black area in the middle is from the laser mirrors for heating.

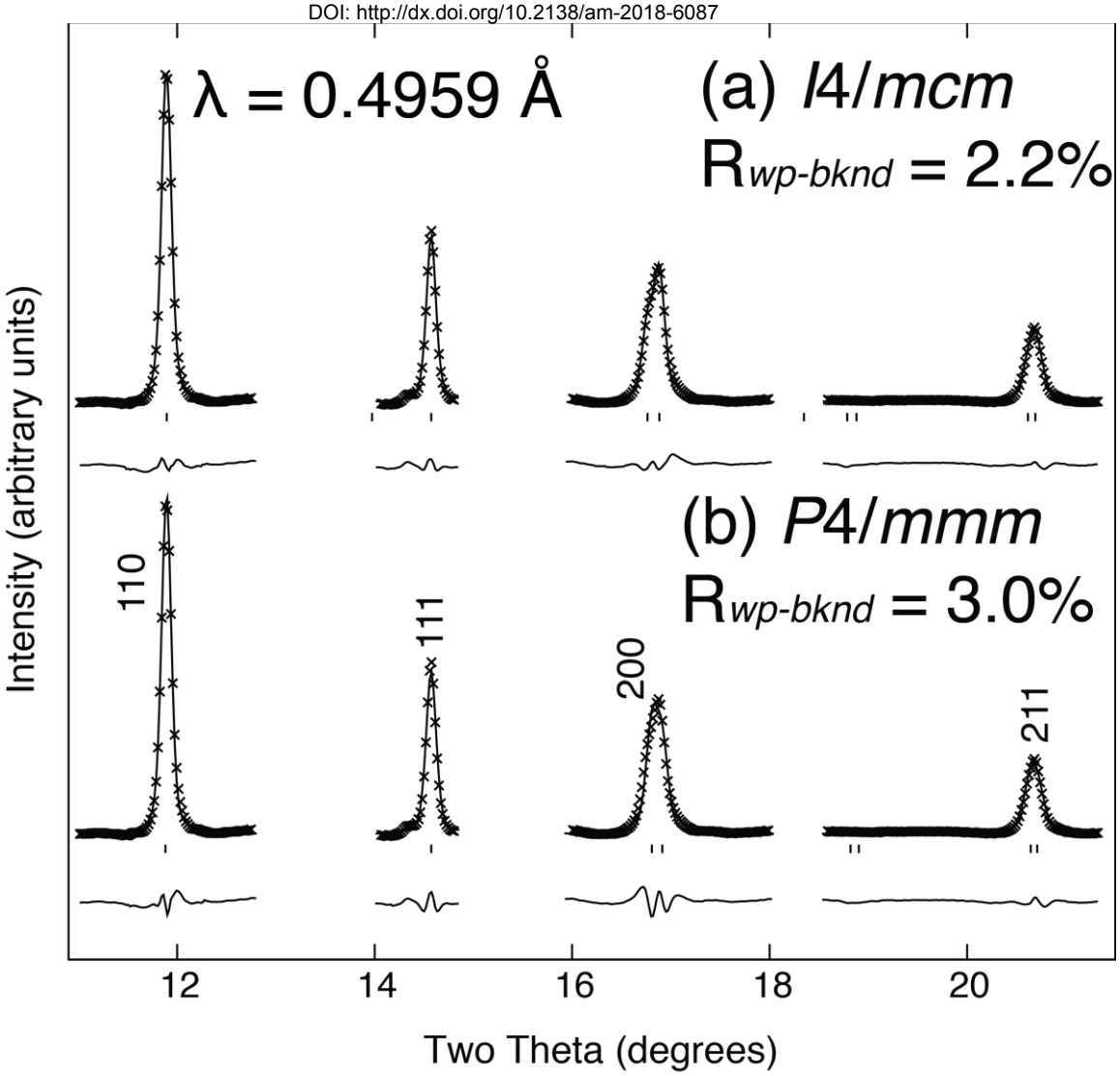

Figure 3: Rietveld refinements of the XRD pattern of CaPv at 53.8 GPa and 300 K with (a) the *I*4/*mcm* and (b) *P*4/*mmm* space groups. The crosses are observed intensities and the line behind crosses is the calculated diffraction patterns. Differences between observed and calculated intensities are plotted below. The small bars represent calculated CaPv peak positions. We did not include the angular ranges for the Pt and Ne peaks in the Rietveld refinements, in order to make $R_{wp\text{-}bknd}$ (residual factor after background subtraction) only sensitive to CaPv.

This is a preprint, the final version is subject to change, of the American Mineralogist (MSA)
Cite as Authors (Year) Title. American Mineralogist, in press.
DOI: http://dx.doi.org/10.2138/am-2018-6087

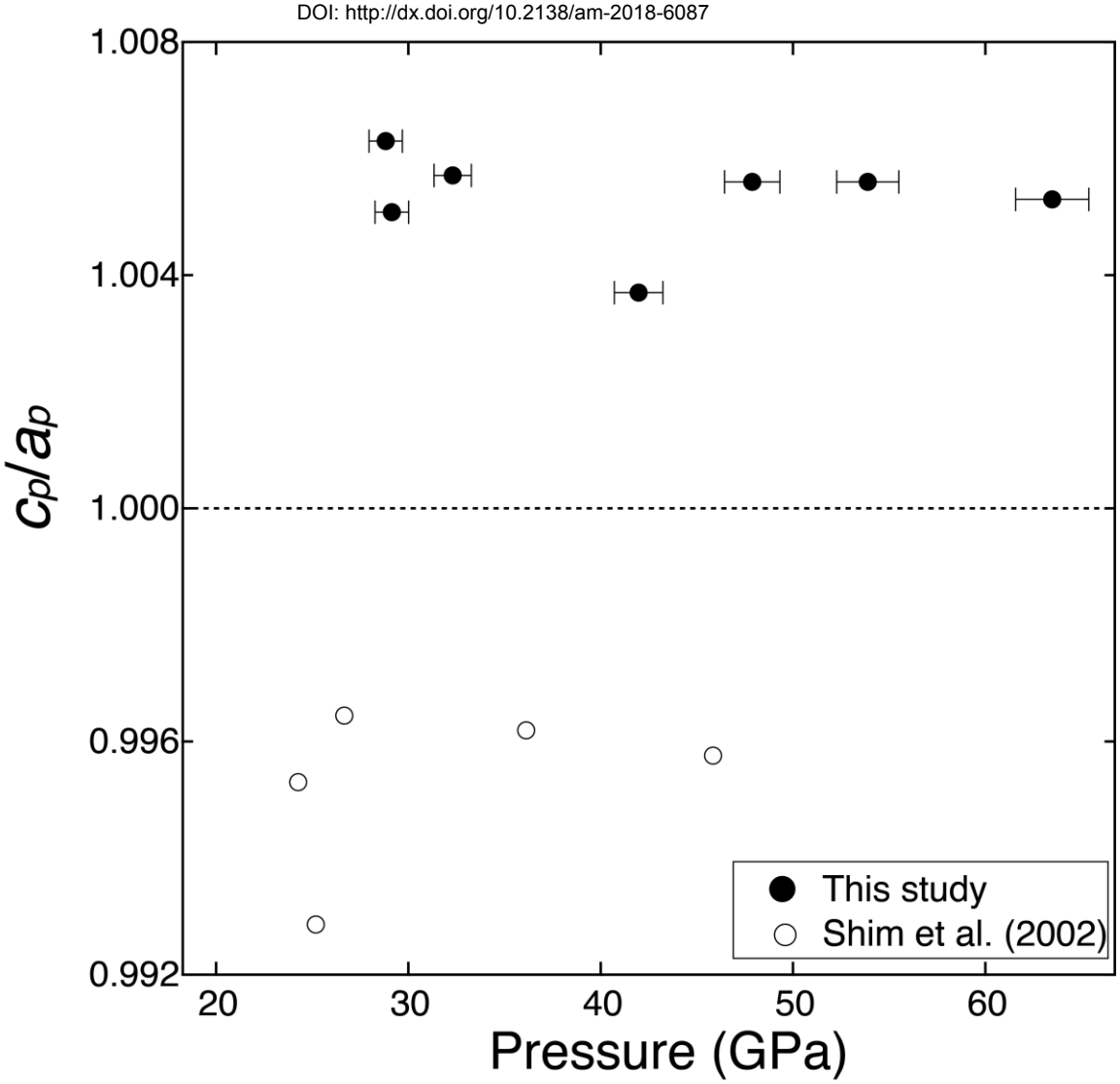

453

454 Figure 4: The axial ratio, c_{pc}/a_{pc}, of the tetragonal CaPv unit cell from Shim et al. (2002)
455 (open circles) and this study (close circles). Error bars represent the estimated 1σ
456 uncertainties.
457

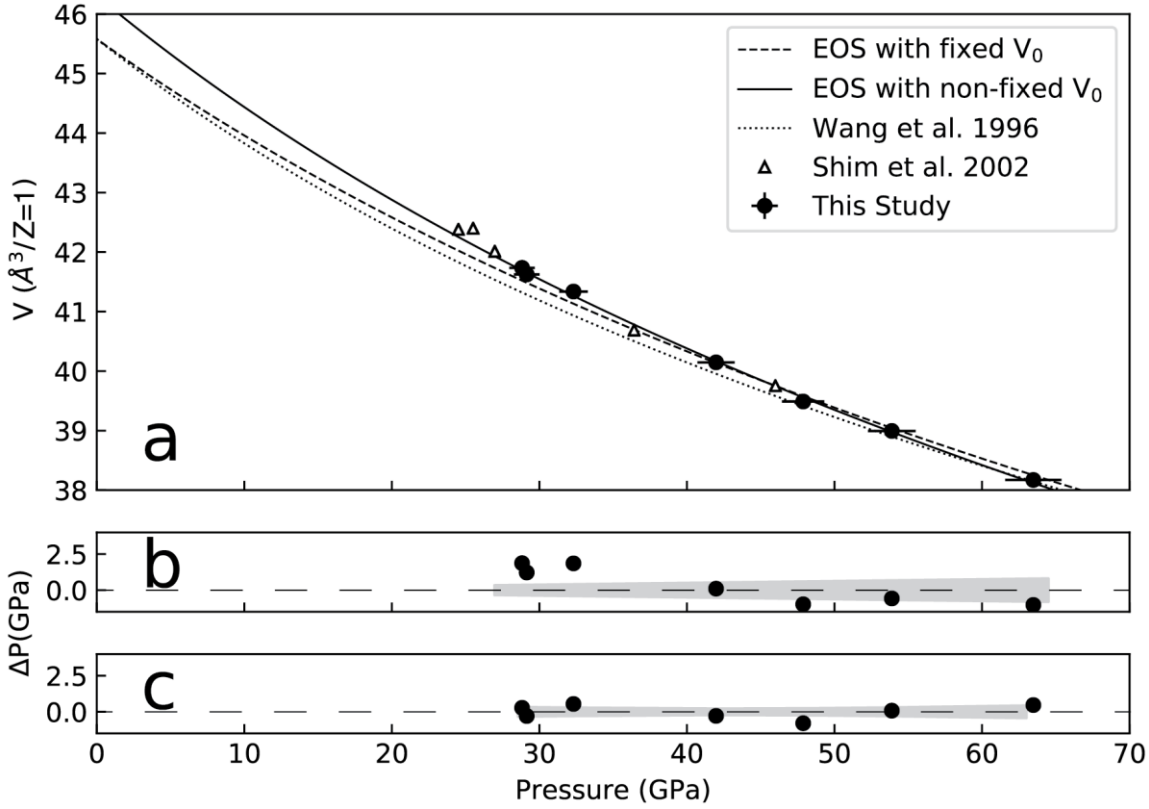

Figure 5: The pseudo-cubic unit cell volume (calculated with the same number of atoms in a unit cell as the *Pm*3*m* structure) of CaPv measured at high pressure (circles). The solid line shows fitting our data to the Vinet equation (Table 2). Pressure was calculated from Ye et al. (2017). We also include the compressional curves from Shim et al. (2002) and Wang et al. (1996) for comparison. Error bars represent estimated 1σ uncertainties. Z is the number of formula unit per unit cell and for pseudo-cubic cell Z is 1. ΔP is the fit residues in pressure with fixed V_0 in (b) or fitted V_0 in (c).

469

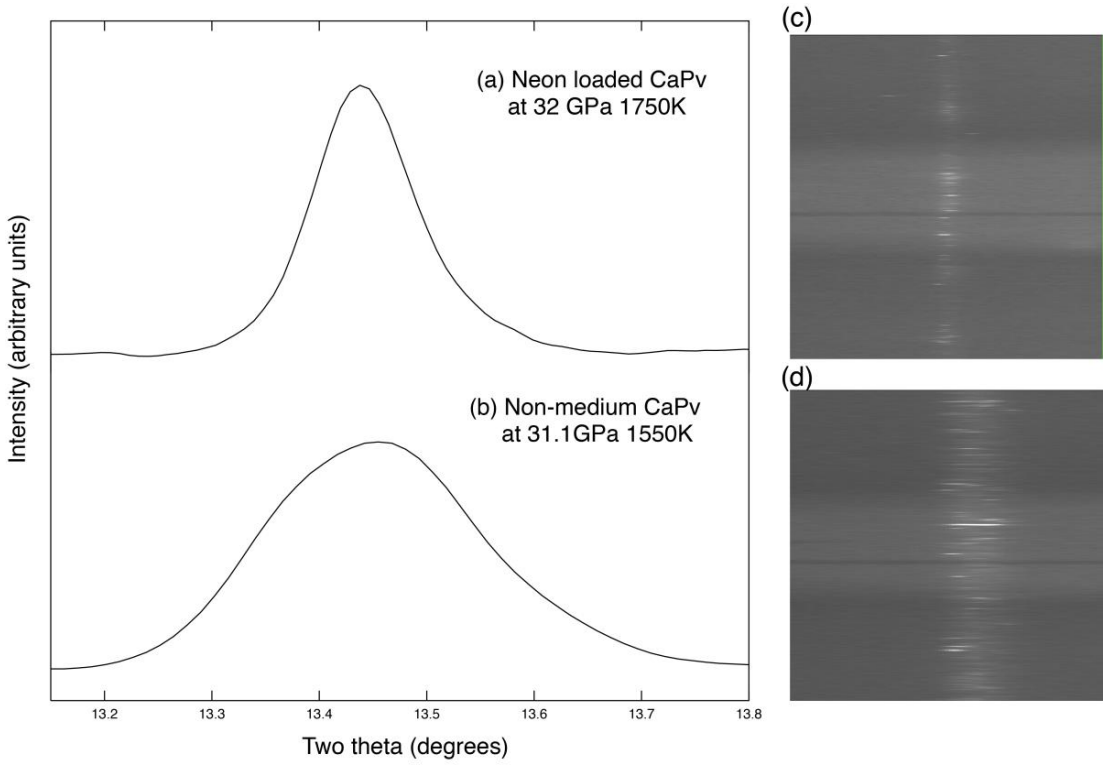

470

471 Figure 6: Cubic 200 diffraction peaks of CaPv measured with (a) Ne and (b) without
472 pressure mediums at in situ high *P* and *T*. The diffraction patterns were measured with
473 an X-ray wavelength of 0.3344 Å and a detector distance of 196.56 mm. Unrolled
474 projection of 2D diffraction area of CaPv 200_{pc} peak (c) with a Ne pressure medium and
475 (d) without a pressure medium with same range (1.4°).

476 **References**:

477 Adams, D.J., and Oganov, A.R. (2006) Ab initio molecular dynamics study of $CaSiO_3$
478 perovskite at P-T conditions of Earth's lower mantle. Physical Review B, 73,
479 184106.

480 Akber-Knutson, S., Bukowinski, M.S.T., and Matas, J. (2002) On the structure and
481 compressibility of $CaSiO_3$ perovskite. Geophysical Research Letters, 29, 4–1.

482 Caracas, R., and Wentzcovitch, R.M. (2006) Theoretical determination of the structures
483 of $CaSiO_3$ perovskites. Acta Crystallographica Section B: Structural Science, 62,
484 1025–1030.

485 Caracas, R., Wentzcovitch, R., Price, G.D., and Brodholt, J. (2005) $CaSiO_3$ perovskite at
486 lower mantle pressures. Geophysical Research Letters, 32, L06306.

487 Chizmeshya, A.V.G., Wolf, G.H., and McMillan, P.F. (1996) First-principles calculation
488 of the equation-of-state, stability, and polar optic modes of $CaSiO_3$ perovskite.
489 Geophysical Research Letters, 23, 2725–2728.

490 Comyn, T.P., McBride, S.P., and Bell, A.J. (2004) Processing and electrical properties of
491 BiFeO3–PbTiO3 ceramics. Materials Letters, 58, 3844–3846.

492 Duffy, T.S., Hemley, R.J., and Mao, H. (1995) Equation of State and Shear Strength at
493 Multimegabar Pressures: Magnesium Oxide to 227 GPa. Physical Review Letters,
494 74, 1371–1374.

495 Fei, Y., Ricolleau, A., Frank, M., Mibe, K., Shen, G., and Prakapenka, V. (2007) Toward
496 an internally consistent pressure scale. Proceedings of the National Academy of
497 Sciences, 104, 9182–9186.

498 Glazer, A.M. (1975) Simple ways of determining perovskite structures. Acta
499 Crystallographica Section A, 31, 756–762.

500 Grocholski, B., Catalli, K., Shim, S.-H., and Prakapenka, V. (2012) Mineralogical effects
501 on the detectability of the postperovskite boundary. Proceedings of the National
502 Academy of Sciences, 109, 2275–2279.

503 Hirose, K., Takafuji, N., Sata, N., and Ohishi, Y. (2005) Phase transition and density of
504 subducted MORB crust in the lower mantle. Earth and Planetary Science Letters,
505 237, 239–251.

506 Holmes, N.C., Moriarty, J.A., Gathers, G.R., and Nellis, W.J. (1989) The equation of
507 state of platinum to 660 GPa (6.6 Mbar). Journal of Applied Physics, 66, 2962–
508 2967.

509 Jung, D.Y., and Oganov, A.R. (2005) Ab initio study of the high-pressure behavior of
510 CaSiO3 perovskite. Physics and Chemistry of Minerals, 32, 146–153.

Kavner, A., and Duffy, T.S. (2001) Pressure–volume–temperature paths in the laser-heated diamond anvil cell. Journal of Applied Physics, 89, 1907–1914.

Kawai, K., and Tsuchiya, T. (2014) P-V-T equation of state of cubic $CaSiO_3$ perovskite from first-principles computation. Journal of Geophysical Research: Solid Earth, 119, 2013JB010905.

Kesson, S.E., Fitz Gerald, J.D., and Shelley, J.M. (1998) Mineralogy and dynamics of a pyrolite lower mantle. Nature, 393, 252–255.

Klotz, S., Chervin, J.-C., Munsch, P., and Marchand, G.L. (2009) Hydrostatic limits of 11 pressure transmitting media. Journal of Physics D: Applied Physics, 42, 075413.

Komabayashi, T., Hirose, K., Sata, N., Ohishi, Y., and Dubrovinsky, L.S. (2007) Phase transition in $CaSiO_3$ perovskite. Earth and Planetary Science Letters, 260, 564–569.

Kurashina, T., Hirose, K., Ono, S., Sata, N., and Ohishi, Y. (2004) Phase transition in Al-bearing $CaSiO_3$ perovskite: implications for seismic discontinuities in the lower mantle. Physics of the Earth and Planetary Interiors, 145, 67–74.

Li, L., Weidner, D.J., Brodholt, J., Alfè, D., David Price, G., Caracas, R., and Wentzcovitch, R. (2006) Elasticity of $CaSiO_3$ perovskite at high pressure and high temperature. Physics of the Earth and Planetary Interiors, 155, 249–259.

Liu, L.-G., and Ringwood, A.E. (1975) Synthesis of a perovskite-type polymorph of $CaSiO_3$, 28, 209–211.

Magyari-Köpe, B., Vitos, L., Grimvall, G., Johansson, B., and Kollár, J. (2002) Low-temperature crystal structure of $CaSiO_3$ perovskite: An ab initio total energy study. Physical Review B, 65, 193107.

Mao, H.K., Chen, L.C., Hemley, R.J., Jephcoat, A.P., Wu, Y., and Bassett, W.A. (1989) Stability and equation of state of CaSiO3-Perovskite to 134 GPa. Journal of Geophysical Research: Solid Earth, 94, 17889–17894.

Margulies, L., Winther, G., and Poulsen, H.F. (2001) In Situ Measurement of Grain Rotation During Deformation of Polycrystals. Science, 291, 2392–2394.

Marquardt, H., Speziale, S., Gleason, A., Sinogeikin, S., Kantor, I., and Prakapenka, V.B. (2013) Brillouin scattering and x-ray diffraction of solid argon to 65 GPa and 700 K: Shear strength of argon at HP/HT. Journal of Applied Physics, 114, 093517.

Meng, Y., Shen, G., and Mao, H.K. (2006) Double-sided laser heating system at HPCAT for in situ x-ray diffraction at high pressures and high temperatures. Journal of Physics: Condensed Matter, 18, S1097.

546 Murakami, M., Hirose, K., Sata, N., and Ohishi, Y. (2005) Post-perovskite phase
547 transition and mineral chemistry in the pyrolitic lowermost mantle. Geophysical
548 Research Letters, 32, L03304.

549 Nisr, C., Ribárik, G., Ungár, T., Vaughan, G.B.M., Cordier, P., and Merkel, S. (2012)
550 High resolution three-dimensional X-ray diffraction study of dislocations in
551 grains of $MgGeO_3$ post-perovskite at 90 GPa. Journal of Geophysical Research:
552 Solid Earth, 117, B03201.

553 Noguchi, M., Komabayashi, T., Hirose, K., and Ohishi, Y. (2013) High-temperature
554 compression experiments of $CaSiO_3$ perovskite to lowermost mantle conditions
555 and its thermal equation of state. Physics and Chemistry of Minerals, 40, 81–91.

556 Ohta, K., Hirose, K., Lay, T., Sata, N., and Ohishi, Y. (2008) Phase transitions in pyrolite
557 and MORB at lowermost mantle conditions: Implications for a MORB-rich pile
558 above the core–mantle boundary. Earth and Planetary Science Letters, 267, 107–
559 117.

560 Ono, S., Ohishi, Y., and Mibe, K. (2004) Phase transition of Ca-perovskite and stability
561 of Al-bearing Mg-perovskite in the lower mantle. American Mineralogist, 89,
562 1480–1485.

563 Ono, S., Ohishi, Y., Isshiki, M., and Watanuki, T. (2005) In situ X-ray observations of
564 phase assemblages in peridotite and basalt compositions at lower mantle
565 conditions: Implications for density of subducted oceanic plate. Journal of
566 Geophysical Research: Solid Earth, 110, B02208.

567 Prakapenka, V.B., Kubo, A., Kuznetsov, A., Laskin, A., Shkurikhin, O., Dera, P., Rivers,
568 M.L., and Sutton, S.R. (2008) Advanced flat top laser heating system for high
569 pressure research at GSECARS: application to the melting behavior of
570 germanium. High Pressure Research, 28, 225–235.

571 Prescher, C., and Prakapenka, V.B. (2015) DIOPTAS: a program for reduction of two-
572 dimensional X-ray diffraction data and data exploration. High Pressure Research,
573 35, 223–230.

574 Ricolleau, A., Fei, Y., Cottrell, E., Watson, H., Deng, L., Zhang, L., Fiquet, G., Auzende,
575 A.-L., Roskosz, M., Morard, G., and others (2009) Density profile of pyrolite
576 under the lower mantle conditions. Geophysical Research Letters, 36, L06302.

577 Ricolleau, A., Perrillat, J.-P., Fiquet, G., Daniel, I., Matas, J., Addad, A., Menguy, N.,
578 Cardon, H., Mezouar, M., and Guignot, N. (2010) Phase relations and equation of
579 state of a natural MORB: Implications for the density profile of subducted oceanic
580 crust in the Earth's lower mantle. Journal of Geophysical Research: Solid Earth,
581 115, B08202.

Rivers, M., Prakapenka, V.B., Kubo, A., Pullins, C., Holl, C.M., and Jacobsen, S.D. (2008) The COMPRES/GSECARS gas-loading system for diamond anvil cells at the Advanced Photon Source. High Pressure Research, 28, 273–292.

Shim, S.-H., Duffy, T.S., and Shen, G. (2000) The stability and P–V–T equation of state of $CaSiO_3$ perovskite in the Earth's lower mantle. Journal of Geophysical Research: Solid Earth, 105, 25955–25968.

Shim, S.-H., Jeanloz, R., and Duffy, T.S. (2002) Tetragonal structure of $CaSiO_3$ perovskite above 20 GPa. Geophysical Research Letters, 29, 2166.

S.-H. Shim (2017) PeakPo - A python software for X-ray diffraction analysis at high pressure and high temperature. Zenodo. http://doi.org/10.5281/zenodo.810199

Stixrude, L., Cohen, R.E., Yu, R.C., and Krakauer, H. (1996) Prediction of phase transition in $CaSiO_3$ perovskite and implications for lower mantle structure. American Mineralogist, 81, 1293–1296.

Stixrude, L., Lithgow-Bertelloni, C., Kiefer, B., and Fumagalli, P. (2007) Phase stability and shear softening in $CaSiO_3$ perovskite at high pressure. Physical Review B, 75, 024108.

Sun, N., Mao, Z., Yan, S., Wu, X., Prakapenka, V.B., and Lin, J.-F. (2016) Confirming a pyrolitic lower mantle using self-consistent pressure scales and new constraints on $CaSiO_3$ perovskite. Journal of Geophysical Research: Solid Earth, 121, 2016JB013062.

Tamai, H., and Yagi, T. (1989) High-pressure and high-temperature phase relations in $CaSiO_3$ and $CaMgSi_2O_6$ and elasticity of perovskite-type CaSiO3. Physics of the Earth and Planetary Interiors, 54, 370–377.

Tangeman, J.A., Phillips, B.L., Navrotsky, A., Weber, J.K.R., Hixson, A.D., and Key, T.S. (2001) Vitreous forsterite (Mg_2SiO_4): Synthesis, structure, and thermochemistry. Geophysical Research Letters, 28, 2517–2520.

Toby, B.H. (2001) EXPGUI, a graphical user interface for GSAS. Journal of Applied Crystallography, 34, 210–213.

Uchida, T., Wang, Y., Nishiyama, N., Funakoshi, K., Kaneko, H., Nozawa, A., Von Dreele, R.B., Rivers, M.L., Sutton, S.R., Yamada, A., and others (2009) Non-cubic crystal symmetry of CaSiO3 perovskite up to 18 GPa and 1600 K. Earth and Planetary Science Letters, 282, 268–274.

Vinet, P., Rose, J.H., Ferrante, J., and Smith, J.R. (1989) Universal features of the equation of state of solids. Journal of Physics: Condensed Matter, 1, 1941.

Wang, Y., Weidner, D.J., and Guyot, F. (1996) Thermal equation of state of $CaSiO_3$ perovskite. Journal of Geophysical Research: Solid Earth, 101, 661–672.

Woodward, P.M. (1997) Octahedral Tilting in Perovskites. I. Geometrical Considerations. Acta Crystallographica Section B: Structural Science, 53, 32–43.

Yashima, M.; Ali, R. (2009) Structural phase transition and octahedral tilting in the calcium titanate perovskite CaTiO3. Solid State Ionics 180, 120-126.

Ye, Y., Prakapenka, V., Meng, Y., and Shim, S.-H. (2017) Inter-comparison of the Gold, Platinum, and MgO Pressure Scales up to 140 GPa and 2,500 K. Journal of Geophysical Research: Solid Earth, 2016JB013811.

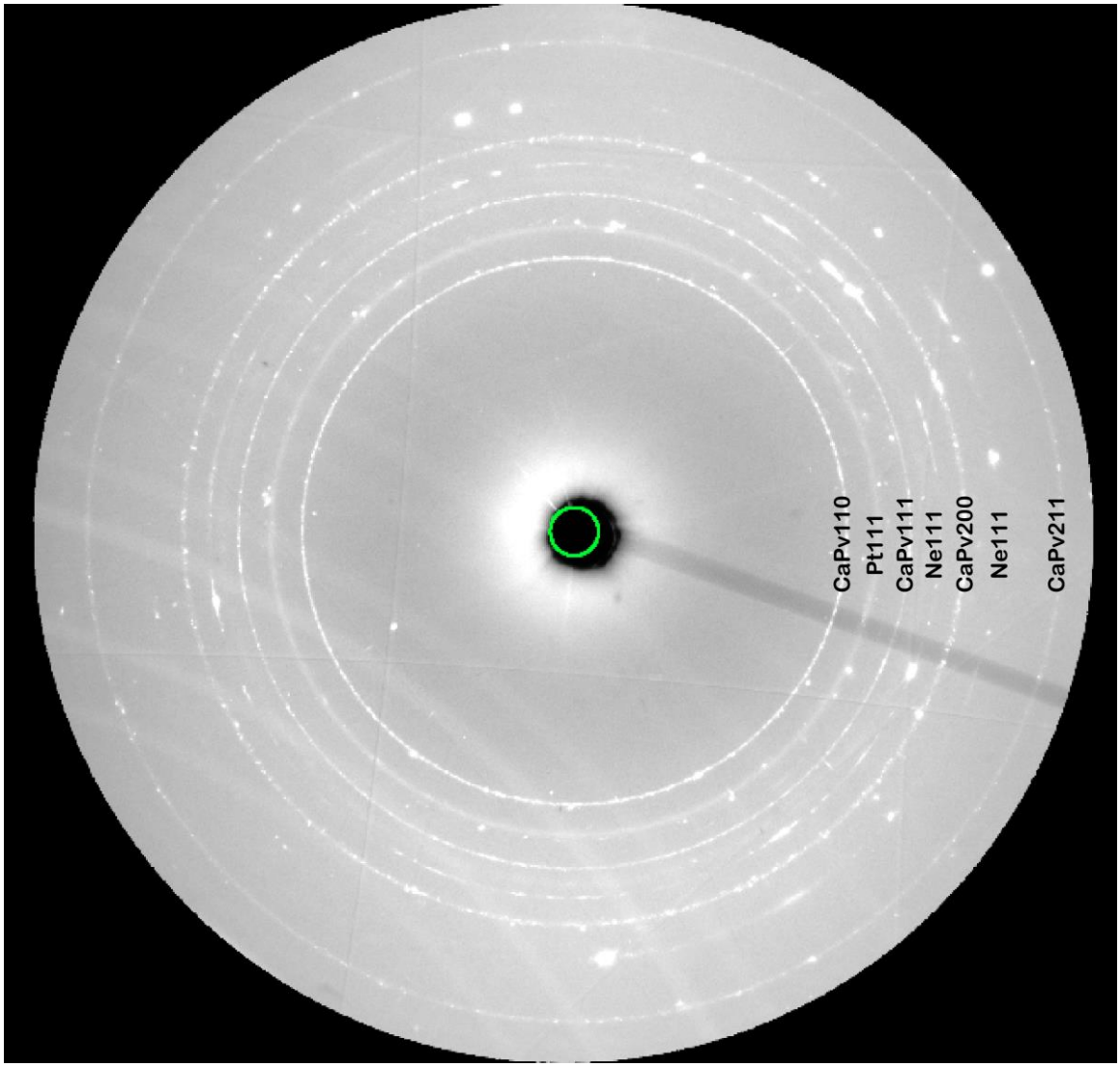

This is a preprint, the final version is subject to change, of the American Mineralogist (MSA)
Cite as Authors (Year) Title. American Mineralogist, in press.
DOI: http://dx.doi.org/10.2138/am-2018-6087

631 Figure S1, 2D diffraction pattern of CaPv, Pt and Neon. We show different diffraction
632 peaks with their Miller indices. We used cubic indices for CaPv. The diffraction pattern
633 was collected at 50 GPa and 300 K.